The Journal of Chemical Physics

Stochastic dynamics of penetrable rods in one dimension: Entangled dynamics and transport properties

Cite as: J. Chem. Phys. **142**, 154906 (2015); https://doi.org/10.1063/1.4918370
Submitted: 02 March 2015 . Accepted: 05 April 2015 . Published Online: 21 April 2015

Galen T. Craven, Alexander V. Popov, and Rigoberto Hernandez

Stochastic dynamics of penetrable rods in one dimension: Entangled dynamics and transport properties

Galen T. Craven, Alexander V. Popov, and Rigoberto Hernandez[a)]
Center for Computational Molecular Science and Technology, School of Chemistry and Biochemistry, Georgia Institute of Technology, Atlanta, Georgia 30332-0400, USA

(Received 2 March 2015; accepted 5 April 2015; published online 21 April 2015)

The dynamical properties of a system of soft rods governed by stochastic hard collisions (SHCs) have been determined over a varying range of softness using molecular dynamics simulations in one dimension and analytic theory. The SHC model allows for interpenetration of the system's constituent particles in the simulations, generating overlapping clustering behavior analogous to the spatial structures observed in systems governed by deterministic bounded potentials. Through variation of an assigned softness parameter δ, the limiting ranges of intermolecular softness are bridged, connecting the limiting ensemble behavior from hard to ideal (completely soft). Various dynamical and structural observables are measured from simulation and compared to developed theoretical values. The spatial properties are found to be well predicted by theories developed for the deterministic penetrable-sphere model with a transformation from energetic to probabilistic arguments. While the overlapping spatial structures are complex, the dynamical properties can be adequately approximated through a theory built on impulsive interactions with Enskog corrections. Our theory suggests that as the softness of interaction is varied toward the ideal limit, correlated collision processes are less important to the energy transfer mechanism, and Markovian processes dominate the evolution of the configuration space ensemble. For interaction softness close to hard limit, collision processes are highly correlated and overlapping spatial configurations give rise to entanglement of single-particle trajectories. © *2015 AIP Publishing LLC.* [http://dx.doi.org/10.1063/1.4918370]

I. INTRODUCTION

The prediction of an atomistic system's macroscopic observables from microscopic physical characteristics is often intractable, either by theory or computation, due to the intrinsic complexity of the underlying dynamical rules or the size of the system. This complexity can be simplified by identifying key mechanisms that drive behavior and considering the system in a reduced representation that captures these mechanisms. One such reduction procedure is coarse-graining (CG) which has received considerable interest due to its success in reproducing all-atom spatial observables with significantly reduced computational resources.[1–3] CG potentials have also been used to model the effective interactions between soft macromolecules at the mesoscale.[4] Such soft matter systems exhibit a large variety of anomalous static and dynamical properties over varying length and time scales. The broad range of these properties enables the optimization over the domain of interactions to result in bespoke materials for many different applications.

In systems for which finite energy costs are accrued when constituents overlap relative to the macromolecular radius of gyration, the effective CG potentials are bounded potentials. Bounded potentials are finite valued at zero separation distinguishing them from atomic interactions which are infinite valued at the origin due to nuclear repulsion. Macromolecular systems such as dendrimers, star polymers, and ring polymers have been modeled using a variety of isotropic soft-core bounded potentials[4–13] that are constructed from a "top-down" coarse-graining procedure.[14]

Perhaps the simplest bounded potential is the penetrable-sphere (PS) model[15]

$$V^{\mathrm{PS}}(r) = \begin{cases} 0, & r > \sigma \\ \epsilon, & r \leq \sigma \end{cases}, \tag{1}$$

where σ is the diameter of the particle and ϵ is a finite energy. The PS model is a limiting case of the generalized exponential model.[16–19] The ubiquitous hard-sphere (HS) potential[20–22] is recovered from the PS model as $\epsilon \to \infty$. In the $\epsilon \to 0$ limit, the interactions are completely ideal. The PS model has been extensively studied analytically and through simulation[23–29] as it provides for a simple theoretical model describing the anomalous structural and dynamical behavior observed in soft-matter systems. Systems governed by bounded interactions can give rise to an interesting phase behavior in which completely repulsive pairwise interactions give rise to multiple occupancy lattice geometries in the formation of "cluster crystals."[10,17,29–31] In molecular dynamics (MD) simulations of the PS model, Santos and coworkers observed anomalous dynamical properties due to this clustering behavior.[26]

While the CG procedure has been shown to be an effective method for modeling structural properties,[2,3] the time-scale acceleration of dynamical observables is a known problem.[32] Several methodologies including dissipative particle dynamics[33] and multi-particle collision dynamics[34,35] have been applied to control thermal fluctuations, and thus the respective time-scale of dynamical evolution through the construction

a)Author to whom correspondence should be addressed. Electronic mail: hernandez@chemistry.gatech.edu.

of renormalized solvent-solute interactions. These simulation protocols allow some control over time- and spatial- scale mismatches arising from a CG procedure.

Here, we develop theory to predict the dynamical properties of a one-dimensional system evolving through the stochastic hard collision (SHC) potential developed in Ref. 36. The SHC model is an alternative to the smooth bounded potentials as the representation for coarse-grained particles. It holds the promise of speeding up molecular dynamics integration because the former does not include explicit long-interactions. In simulation, a softness parameter $\delta \in [0,1]$ bridges hard rod (HR) ($\delta = 0$) and the ideal ($\delta = 1$) behavior limits. We find that while the spatial properties are complex,[37] the dynamical properties can be predicted using Enskog corrections to Boltzmann kinetic theory. As shown in Fig. 1, the value of δ has a significant influence on the dynamical behavior. In the HR limit, the system remains well-ordered over time, experiencing only nearest-neighbor interactions, as illustrated by trajectories in Fig. 1(a). In the ideal limit, the particles never interact, and each particle moves ballistically as shown in Fig. 1(d). For intermediate values of δ, as shown Figs. 1(b) and 1(c), complex interaction networks are generated and single-particle trajectories become entangled. The aim of this article is to understand the effect that these entangled interaction networks have on the system's dynamical observables.

One-dimensional systems are often studied because they are analytically tractable.[38–41] These analytic results provide insight into more realistic systems in higher dimensions. The equation of state for the HR system was solved exactly by Tonks[42] and thus, this system is colloquially known as a Tonks gas. Further theoretical studies of the nonequilibrium properties of the HR system have also been performed, notably by Lebowitz *et al.*[43–45] and Jepsen.[46] These theoretical predictions have been confirmed by Bishop and Berne,[47] as well as Haus and Raveché,[48] using molecular dynamics simulations.

The remainder of this article is organized as follows: in Sec. II, details of the applied simulation methodology are presented. Sections III and IV contain theory and numerical results for the structural and dynamical properties, respectively, of a system of penetrable rods modeled by the SHC potential. In Sec. V, the rate of sequential mixing is measured from simulation and related to diffusional rates in configuration space.

II. MODEL AND SIMULATION DETAILS

MD simulations have been performed on a system of $N = 200$ stochastically penetrable rods using a codebase developed in-house. Each rod has a length σ and mass m and is constrained to move under periodic boundary conditions on a line of length L_x. The initial velocities are sampled randomly from a Boltzmann distribution and initial positions of each particle are chosen by placing each particle's center of mass on a uniform lattice. Throughout this article, values of the reported observables are reduced using σ and $\tau = \sigma/\sqrt{k_B T/m}$. Using standard linear scaling, after the initial velocities are assigned, these velocities are rescaled such that the energy of the system, for every trajectory, is $Nk_BT/2$.

The dynamics of the system of rods are evolved through the SHC algorithm introduced in Ref. 36. At the time t_{col} of a possible hard collision between two particles i and j, a random number a_{ij} is generated and compared to a predefined softness parameter δ. The softness parameter is invariant during the duration of the simulation. If $a_{ij} > \delta$, the pair of particles collides elastically and if $a_{ij} < \delta$, there is no interaction between that pair of particles. This algorithm generates an isotropic stochastic bounded potential,

$$V_{ij}^{\text{SHC}}(r) = \begin{cases} 0, & r > \sigma \\ 0, & r \le \sigma \text{ and } a_{ij}(t_{\text{col}}) < \delta \\ \infty, & r \le \sigma \text{ and } a_{ij}(t_{\text{col}}) > \delta \end{cases}. \tag{2}$$

When $\delta = 0$, the dynamics of a system evolving through (2) is that of a HR system and when $\delta = 1$ that of an ideal gas with no interaction between particles.

Each pairwise interaction is either hard or soft and can change many times throughout the duration of the simulation. The time-dependence of the SHC connection network can be expressed as a symmetric adjacency matrix,

$$\mathbf{S}(t) = \begin{pmatrix} s_{11} & s_{12} & \cdots & s_{1N} \\ s_{21} & s_{22} & \cdots & s_{2N} \\ \vdots & \vdots & \ddots & \vdots \\ s_{N1} & s_{N2} & \cdots & s_{NN} \end{pmatrix}, \tag{3}$$

in which each s_{ij} is a time-varying indicator taking values 1 or 0 depending on whether the pairwise connection between

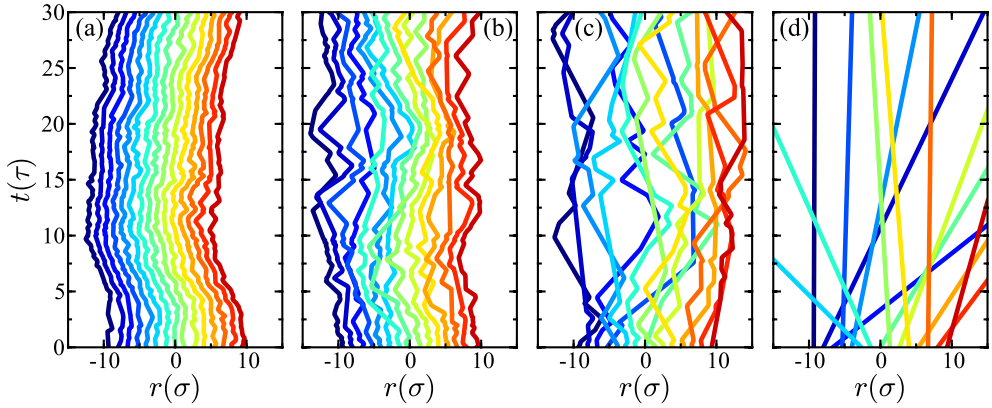

FIG. 1. Representative trajectories of 15 initially neighboring particles interacting through Eq. (2) for (a) $\delta = 0.0$, (b) $\delta = 0.05$, (c) $\delta = 0.5$, and (d) $\delta = 1.0$ at $\phi_0 = 0.75$. The trajectory of each particle is shown in a different color. The x-axis shows the particles position in reduced units r/σ and the y-axis shows time in reduced units t/τ.

particles i and j is hard or ideal, respectively. Through Eq. (3) and the hard sphere potential,

$$V^{\mathrm{HS}}(r) = \begin{cases} 0, & r > \sigma \\ \infty, & r \leq \sigma \end{cases}, \tag{4}$$

the single-particle phase space point $\Gamma = (r_i, v_i)$ evolves ballistically, subject to the exclusion condition: $|r_i(t) - r_j(t)| > \sigma$ when $s_{ij}(t) = 1$.[49] In simulation, before a sampling phase was initiated, the system was aged for at least 10^5 total (hard and soft) interactions to generate a spatially relaxed state.

The occupied volume fraction for the SHC model when no particles overlap ($\delta = 0$) is

$$\phi_0 = \frac{N\sigma}{L_x}. \tag{5}$$

For $\delta > 0$, the rods are allowed to overlap and the effective volume fraction ϕ is less than that of the HR case. Allowing interpenetrability by varying the softness of the interaction generates complex behavior in ϕ[26,36,37,50] and as we show below, these density fluctuations manifest in similar behavior in the system's dynamical evolution. Throughout this article, we express the dynamical properties as a function of hard occupied volume fraction ϕ_0 and interparticle softness δ.

III. STRUCTURAL PROPERTIES

A. Radial distribution function (RDF)

The structure of the liquid phase of the SHC particles can be classified through the RDF $g_2(r)$ and serves as a reference for the dynamics discussed below. Earlier,[36,37] we observed that the RDF for the SHC particles is the same as that for the corresponding soft particle system, and provide clearer demonstration with additional analytic theory below. Specifically, the RDF at positive contact $g_2(\sigma^+)$ and the multi-body softness parameter ζ, presented in Ref. 36, appear in the theoretical expressions for the transport properties derived herein. An exact analytic expression for the RDF of the HR model was derived by Salsburg, Zwanzig, and Kirkwood.[51] This theoretical prediction has been shown to agree with results obtained from MD simulations[47,48] and provides insight into the statistical geometries of the liquid structures induced by short-range interaction potentials.

The softness parameter δ has a large influence on the functional form of the RDF. Therefore, for the SHC model, g_2 is parametrized by δ, i.e., $g_2 \equiv g_2(r;\delta)$. The known positive contact values of the RDF at the limiting values of δ are

$$g_2(\sigma^+;0) = \frac{1}{1-\phi_0}$$

and

$$g_2(\sigma^+;1) = 1, \tag{6}$$

for a Tonks gas and an ideal gas, respectively. These expressions are valid at the thermodynamic limit. In SHC systems, the ratio of negative flow to positive flow at the boundary of the penetrative region ($0 \leq r \leq \sigma$) is equal to δ, i.e.,

$$\delta = \frac{g_2(\sigma^-;\delta)}{g_2(\sigma^+;\delta)}, \tag{7}$$

where $g_2(\sigma^-;\delta)$ is the value of the RDF at negative contact.

Malijevsky and Santos[23] (MS) have derived an expression for the RDF of the PS model in one dimension termed the "low-temperature approximation" (LTA). Adapting this derivation for the SHC model by converting the energetic distributions to probabilistic collision arguments in terms of δ gives

$$g_2(r;\delta) = \frac{r-\sigma}{\sigma} C_0(\delta)\Theta\left(\frac{\sigma - r}{\sigma}\right) + \sum_{n=0}^{\infty} \psi_n\left(\frac{r-n\sigma}{\sigma}\right)\Theta\left(\frac{r-n\sigma}{\sigma}\right), \tag{8}$$

where

$$C_0(\delta) = \frac{\delta}{\phi_0}\epsilon_1(\epsilon_0 - \epsilon_1) \tag{9}$$

and

$$\psi_n(r) = \exp\left[-\epsilon_1 r\right]\frac{1}{\phi_0}\frac{r^{n-1}}{n!}(n + (\epsilon_0 - \epsilon_1)r)\epsilon_1^n. \tag{10}$$

In the equations above, ϵ_1 is defined in terms of ϵ_0 as

$$\epsilon_1 \equiv \frac{\epsilon_0 - \phi_0}{\phi_0}, \tag{11}$$

and is obtained by solving the equation

$$\epsilon_1 = \frac{1-\delta}{\delta}((\phi_0 - 1)\epsilon_1 + \phi_0)\exp\left[-\epsilon_1\right]. \tag{12}$$

Equations (8)–(11) constitute the LTA of MS for g_2, adapted for the SHC model.

Equation (8) gives an excellent approximation to the RDF in Fig. 2 across all values of δ over the presented densities. Although not shown, the agreement between Eq. (8) and the results measured from simulation begins to diverge at densities above maximum HR packing fraction ($\phi_0 > 1$) and small-δ values. Full explanations of the observed functional forms including the characteristic convexity observed for $r < \sigma$ can be found in Refs. 36 and 37. The agreement observed between the two models is surprising: in the PS model, particles evolve through Hamiltonian equations of motion and the probability of a pair overlapping is dependent on the relative velocity at the moment of collision. This differs from the SHC model in which the kinetic energy plays no role in the penetration probability. Moreover, we conjecture that the SHC model samples the exact configuration integral of the PS model.

By taking the one-sided limit of Eq. (8) as σ is approached from the positive direction, the RDF value at positive contact

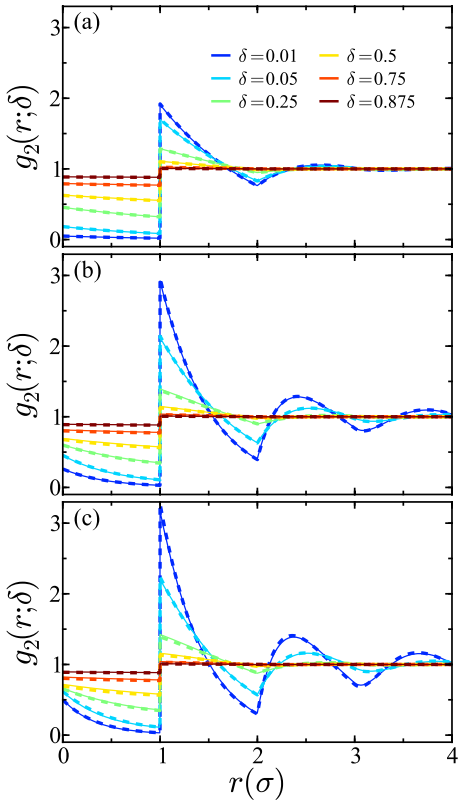

FIG. 2. The radial distribution function for (a) $\phi_0 = 0.5$, (b) $\phi_0 = 0.75$, and (c) $\phi_0 = 0.85$ and various values of δ. The solid line is the result of MD simulations. The dashed line is the results given by Eq. (8).

$$g_2(\sigma^+;\epsilon_0(\delta)) = \frac{\epsilon_0 - \phi_0 + \exp[1-\epsilon_0/\phi_0](\phi_0\epsilon_0 - \epsilon_0 + \phi_0)}{\phi_0^2} \tag{13}$$

can be expressed in terms of ϕ_0 and ϵ_0. The known contact values in the HR ($\delta = 0$) and ideal ($\delta = 1$) limits can also be recovered from Eq. (13).

B. Solvation shells and multi-body softness

As the density of the SHC system is increased toward the maximum HR packing fraction, multi-body interactions contribute significantly to the pairwise potential of mean force (PMF) $w_2(r;\delta)$. The PMF is defined in terms of $g_2(r;\delta)$ by

$$w_2(r;\delta) = -\frac{1}{\beta}\ln\left[g_2(r;\delta)\right], \tag{14}$$

where $\beta = 1/k_BT$. These structural transitions can be observed by comparing Fig. 2(a) with Fig. 2(c), in which, for large-δ values, the pairwise behavior is highly uncorrelated. At small-δ values and high density ($\phi_0 = 0.85$), the pairwise structure is highly correlated and g_2 exhibits multiple solvation shells.

The pairwise softness δ is not sufficient to describe the induced multi-body effects observed in each solvation shell with increasing density because the system becomes too highly correlated.[36,37] With the center of a particle as the origin, we define the nth shell as the physical space over the radial interval $\mathcal{S}_n = [n\sigma,(n+1)\sigma] : n \in \mathbb{Z}^\star$. The probability to find another particle in $\mathcal{S}_n$, relative to the corresponding ideal gas density over the same interval,

$$\zeta_n(\delta) = \frac{\int_{n\sigma}^{(n+1)\sigma} e^{-\beta w_2(r;\delta)}\,dr}{\int_{n\sigma}^{(n+1)\sigma} e^{-\beta w_2(r;1)}\,dr}, \tag{15}$$

is a metric for the degree of structural correlation. Of particular importance is the interval defining the zeroth solvation shell $\mathcal{S}_0$. We use the "zeroth" naming convention as it is common in a Tonks gas to define $[\sigma,2\sigma]$ as the first solvation shell. Note that the discontinuity at $r = \sigma$ for $\delta \neq 1$ is handled through the usual methods for improper integrals.[52] Evaluating Eq. (15) over $\mathcal{S}_0$ defines the multi-body softness ζ_0, i.e., the multi-body induced probability to find a particle at $r < \sigma$ relative to corresponding ideal gas density.

Construction of geometric correlation functions[53]—such as the occupied volume fraction ϕ—for the SHC model, rely on the mapping $\delta \to \zeta_0$. Combining Eqs. (8), (14), and (15), ζ_0 can be expressed in closed form as

$$\zeta_0(\delta) = \frac{1+\epsilon_0-\epsilon_0/\phi_0}{2\phi_0}\left(\delta - \delta\epsilon_0/\phi_0 + \frac{2\phi_0(1-\exp[1-\epsilon_0/\phi_0])}{\epsilon_0-\phi_0}\right). \tag{16}$$

Equation (15) can be evaluated for higher-order solvation shells ($n > 0$), however, due to increasing algebraic complexity we refrain from reproducing those expressions here.

As the limiting cases are approached, the known values ($\zeta_0(0) = 0$ and $\zeta_0(1) = 1$) are recovered through Eq. (16). Comparisons between the theoretical prediction for ζ_0 and the empirical result in Fig. 3 are in excellent agreement. We have previously derived an expression for the effective volume fraction ϕ which relied on empirically measured values of ζ_0.[36] The agreement observed between Eq. (16) and the measured values suggests that for a one-dimensional SHC system, ϕ can now be predicted without any empirical parameterization. We will show in Sec. IV C that ζ_0 can also be used as a basis for accurate approximations of the transport properties of the SHC system.

The interplay between softness and density produces emergent structural behavior over the hierarchy of solvation shells. At the Poisson distributed ($\delta = 1$) limit, the density is uniform over all $\mathcal{S}_n$. As δ is moved away from this limit, structural correlations emerge. Variations in local density give rise to the emergence of distinct structures. These transitions can be quantified through analysis of the degree of correlation

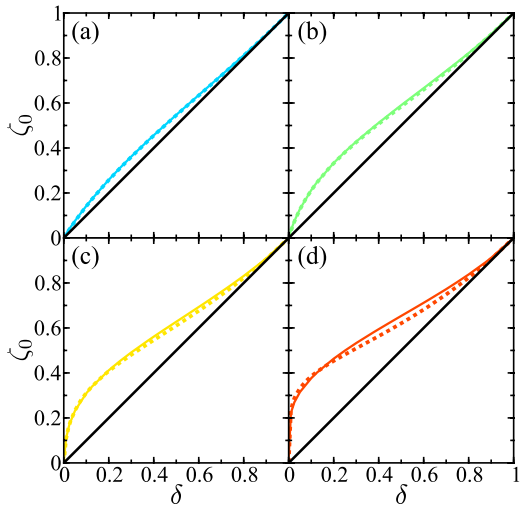

FIG. 3. ζ_0 as a function of δ for (a) $\phi_0 = 0.25$, (b) $\phi_0 = 0.5$, (c) $\phi_0 = 0.75$, and (d) $\phi_0 = 0.95$. In each panel, the solid curve is the result measured from MD simulations and the dashed curve is the result given by Eq. (16). The thick solid line (black) corresponds to the infinite dilution limit where $\zeta_0 = \delta$.

in each shell. While the zeroth order shell provides the most distinct variation in behavior as illustrated in Fig. 4(a), for $n > 0$ the removal or addition of density from each shell gives insight into the assembly process, or lack thereof.

As illustrated in Fig. 4(b), for $\delta = 0.75$, the density remains approximately uniform in higher-order shells over all values of ϕ_0 even above the maximum HR packing fraction. Thus, for large values of δ the system contains only small correlations, and the transition into a structural regime becomes increasingly indistinct with increasing density. The latter can be observed in Fig. 4(a) through the approximately linear density dependence of ζ_0 for $\delta = 0.75$. The results in the opposite small δ (=0.01) regime are shown in Fig. 4(e). For $\phi_0 = 0.5$, the density variation is predominantly in $\mathcal{S}_1$, and $\mathcal{S}_0$ differs only slightly from the ideal $\zeta_0 = \delta$ value. For large values of ϕ_0, the local density is more highly partitioned into $\mathcal{S}_0$, $\mathcal{S}_2$ and $\mathcal{S}_3$. In this case, particle density is effectively removed from $\mathcal{S}_1$, $\mathcal{S}_4$, and higher-order shells, increasing the degree of local correlation inside the penetrative region. Thus, for small values δ we do observe an emergent structural transition. The onset of this transition can be observed in Fig. 4(a), characterized by the sigmoid shape of the ζ_0 curve for $\delta = 0.01$.

By evaluating Eq. (15) using Eq. (8) over the corresponding solvation shell, ζ_n can be calculated analytically. The predicted values shown in Figs. 4(b)-4(e) for $\phi_0 < 0.95$ are in excellent agreement with simulation in liquid-like density regimes. This suffices for applications to solvent mediated reactions at CG length-scales, all of which occur well below the density where the theory begins to deviate from the simulation.

C. Translational order parameters

The degree of pairwise translational order in the SHC system can be quantified through the structural order parameter[54,55]

$$-s_2(\delta) = \frac{\phi_0}{\sigma}\int_0^\infty g_2(r;\delta)\ln g_2(r;\delta) - [g_2(r;\delta) - 1]\,dr. \quad (17)$$

As illustrated in Fig. 5(a), the values of $-s_2$ computed for SHC systems over a broad domain of δ increase monotonically with ϕ_0. This suggests a similarity to simple fluids, as they exhibit the same trend. Moreover, in a one-dimensional SHC system, we observe no anomalous clustering behavior, as would have been indicated by a turnover in $-s_2$. Anomalous structural transitions have been previously observed in the Gaussian-core fluid[56] and the SHC model in three dimensions, as indicated by the observation of a turnover in the value of ζ. The absence of such a transition in the one-dimensional SHC model agrees with the findings in our earlier work.[37]

Truskett and co-workers[56,57] have suggested the use of the cumulative structural order integral

$$I_{s_2}(r;\delta) = \frac{\phi_0}{\sigma}\int_0^r g_2(r';\delta)\ln g_2(r';\delta) - [g_2(r';\delta) - 1]\,dr' \quad (18)$$

to measure the contribution that each coordination shell has on the total pairwise order. As illustrated in Fig. 5(b), for densities close to and greater than the maximum HR packing fraction ($\phi_0 > 0.95$), there is less correlation inside the core region than that observed at lower densities. Thus, overlapping rods become less correlated with increasing density at small values of δ and r. This decorrelation is caused by caging

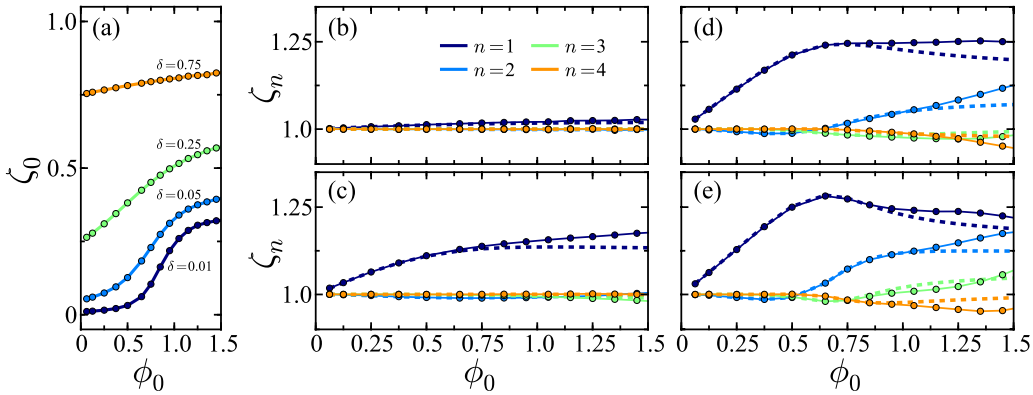

FIG. 4. (a) The measured value of ζ_0 as a function of ϕ_0 for various δ values as marked. ζ_n as a function of ϕ_0 for (b) $\delta = 0.75$, (c) $\delta = 0.25$, (d) $\delta = 0.05$, and (e) $\delta = 0.01$ over the intervals of the corresponding solvation shell $\mathcal{S}_n$ for $n \in \{1, 2, 3, 4\}$. The solid curves are the results measured from MD simulations and the dashed curves are obtained from Eq. (15) using Eq. (8) over the corresponding solvation shell.

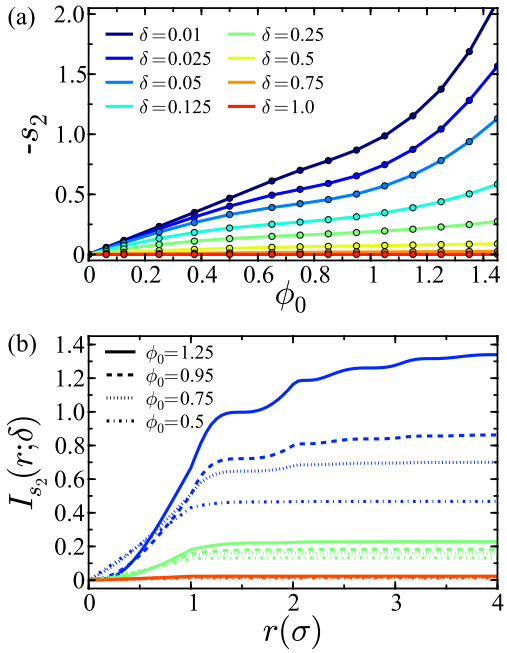

FIG. 5. (a) The pairwise structural order parameter $-s_2$ as a function of ϕ_0 for various values of δ. (b) The cumulative order integral $I_{s_2}(r;\delta)$ at $\delta = 0.01$ (blue), $\delta = 0.25$ (green), and $\delta = 0.75$ (red) for $\phi_0 \in \{0.5, 0.75, 0.95, 1.25\}$.

effects where a cluster of overlapping particles are forced into heavily overlapped states by the shell of particles surrounding the cluster.

IV. TRANSPORT PROPERTIES

Bishop and Berne performed computer simulations of a one-dimensional HR system[47] and confirmed earlier theoretical predictions with respect to the dimensional scaling behavior of dynamical properties. The results of these experiments contradicted earlier predictions by Alder and Wainwright[58] who used pioneering methods of computer simulation to predict the observables of hard body systems in higher dimensions.[59] The transport properties of the PS model in three dimensions have also been studied through the use of MD simulations by Suh *et al.*[26,60] These simulations elucidate the influence anomalous clustering behavior has on transport properties and further suggest structural and dynamical measurables that are ill defined in hard body systems but useful for describing soft systems. All of these measures together serve as a useful benchmark to characterize the dynamical behavior of the SHC particles and the degree to which they behave like soft or hard particles with varying softness parameter δ.

A. Collision frequency

There are two types of "collisions" between pairs of particles in the SHC algorithm: (1) hard elastic collisions that are analogous to those observed in hard-body systems, and (2) extremely soft collisions in which there is no repulsion between a given pair of particles. For simplicity, we refer to these as hard and soft interactions, respectively. Note that our definition of soft collisions differs with that used by Santos and coworkers[26] to characterize MD simulations of the PS model, wherein they define soft collisions as those that involve refractive-type interactions.

The mean free path λ, defined as the average distance a single particle travels between collisions, is the characteristic length scale of ballistic motion. In systems evolving through continuous potentials, particularly in the liquid state, particles constantly interact and the notion of discrete and impulsive events, i.e, collisions, is ill-defined. For hard-edge potentials, such as the HS, PS, and SHC models, the free path can be readily defined. Its value is directly related to the collision frequency ω and the rate of temporal decorrelation governing transport properties.

Boltzmann kinetic theory predicts that for a system of rarefied HRs in one dimension, the mean free path is

$$\lambda_B = \frac{\sigma}{\sqrt{2}\phi_0}. \tag{19}$$

This results from the fact that $g_2(r)$ is a step function satisfying the condition that $g_2(\sigma^+) = 1$ at infinite dilution. As the density of the system is increased from this limit, the constituent particles take on a structured state and Eq. (19) must be modified by the Enskog factor χ,[26,61]

$$\lambda_h = \frac{\lambda_B}{\chi}, \tag{20}$$

where $\chi = g_2(\sigma^+)$ is the radial distribution function at positive contact. For finite densities ($\phi_0 > 0$), $g_2(\sigma^+) \neq 1$ and $\lambda_h < \lambda_B$. The latter arises from the density-dependent intrinsic structure of the constituent particles.

In systems evolving through the stochastic collision rules defined by Eq. (2), the softness δ has a large effect on the static structure and hence on the RDF at positive contact $g_2(\sigma^+;\delta)$. Due to the stochastic collision probability, Eq. (20) must be modified by a factor $(1-\delta)$ giving

$$\lambda_h(\delta) = \frac{\sigma}{\sqrt{2}\phi_0}\left(\frac{1}{(1-\delta)g_2(\sigma^+;\delta)}\right), \tag{21}$$

which is the Enskog-modified mean free path for a system evolving under the stochastic potential (2).

The frequency of hard collisions for a single particle can be expressed through Eq. (21) and the average speed $\langle v\rangle = \sqrt{2k_BT/\pi m}$ of a one-dimensional Maxwellian system as

$$\omega_h = \frac{\langle v\rangle}{\lambda_h}. \tag{22}$$

The frequency of soft collisions,

$$\omega_s = \frac{\langle v\rangle}{\lambda_B} g_2(\sigma^-;\delta), \tag{23}$$

depends on λ_B and the RDF at negative contact $g_2(\sigma^-;\delta)$. Note that a mean free path for a soft-particle system is ill-defined because of the long-range nature of the interaction potential. The total collision frequency

$$\omega_{tot} = \omega_h + \omega_s \tag{24}$$

can therefore be expressed in terms of the positive and negative RDF contact values,

$$\omega_{tot}(\delta) = \frac{\langle v\rangle}{\lambda_B}\left(\frac{g_2(\sigma^+;\delta)}{g_2(\sigma^-;\delta)\,(g_2(\sigma^+;\delta) - g_2(\sigma^-;\delta))}\right). \tag{25}$$

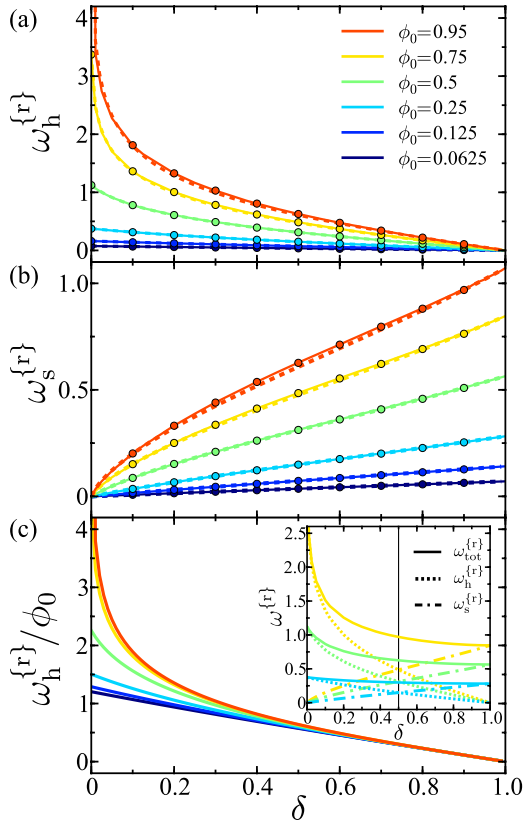

FIG. 6. (a) The reduced hard collision frequency $\omega_h^{\{r\}} = \omega_h\tau$ as a function of δ. (b) The reduced soft collision frequency $\omega_s^{\{r\}} = \omega_s\tau$ as a function of δ. For both (a) and (b), the curves given by Eqs. (22) and (23), respectively, are shown using empirical values (solid) and theoretical values (dashed) for $g_2(\sigma^+;\delta)$. The circles are the results measured from MD simulations. (c) The reduced hard collision frequency scaled by ϕ_0 as a function of δ. Inset is the reduced total collision frequency $\omega_{tot}^{\{r\}}$ measured from simulation. The solid vertical line ($\delta = 0.5$) is the point where $\omega_h^{\{r\}} = \omega_s^{\{r\}}$. In all panels, the colors correspond to respective ϕ_0 values shown in the legend of (a).

To calculate the collision frequency from simulation, 100 trajectories were propagated for each parameter set $\{\phi_0, \delta\}$. After the initial relaxation phase described in Sec. II, each trajectory was computed until 10^5 collisions had occurred and ω was calculated over these collisions. The theoretical and simulated collision frequencies are shown in Fig. 6. While ω_s is an approximately linear function of δ, ω_h is highly nonlinear in the small-δ regime at large densities. The scaled hard collision frequencies, ω_h/ϕ_0, shown in Fig. 6(c), illustrate the result that the hard collision frequency does not scale linearly with density. The measured results for total collision frequency ω_{tot} are shown in the inset in Fig. 6(c). As expected, for $\delta = 0.5$, the hard and soft collision frequencies agree, i.e., $\omega_h = \omega_s$.

B. Velocity autocorrelation function

For an infinite system of hard point particles with Maxwellian distributed velocities, Jepsen[46] presented an exact solution for the normalized velocity autocorrelation function (VACF),

$$\psi(t) = \frac{\langle v_x(0)v_x(t)\rangle}{\langle v_x(0)v_x(0)\rangle}, \tag{26}$$

and predicted an asymptotic decay with a negative tail scaling as t^{-3}. This result was later confirmed in simulation.[47,48] Lebowitz *et al.* predicted that the short-time decay of a HR system could be well approximated by an exponential function whose rate constant is proportional to the HR collision frequency $\omega_h(0)$. Following the prediction by Lebowitz *et al.* and the Enskog prediction for the decay rate of an uncorrelated collision process, a natural approximation for the VACF of the SHC model is

$$\psi_E(\delta;t) = e^{-2\omega_h(\delta)t}, \tag{27}$$

where $\omega_h(\delta)$ is the hard collision frequency given by Eq. (22). This exponential decay is observed in other systems such as a Langevin equation with Markovian noise.

A comparison between the values for the VACF measured from simulation and predicted by Eq. (27) is shown in Fig. 7 for various values of ϕ_0 and δ. The MD simulations were performed in the *NVEP* ensemble which is achieved by setting the total momentum of the system to zero through standard velocity scaling procedures.[62] In the liquid-like density regimes, both results are in agreement. Moreover, the short-time decay of the VACF is approximately exponential for all values of δ, while the long-time decay shows exponential behavior only

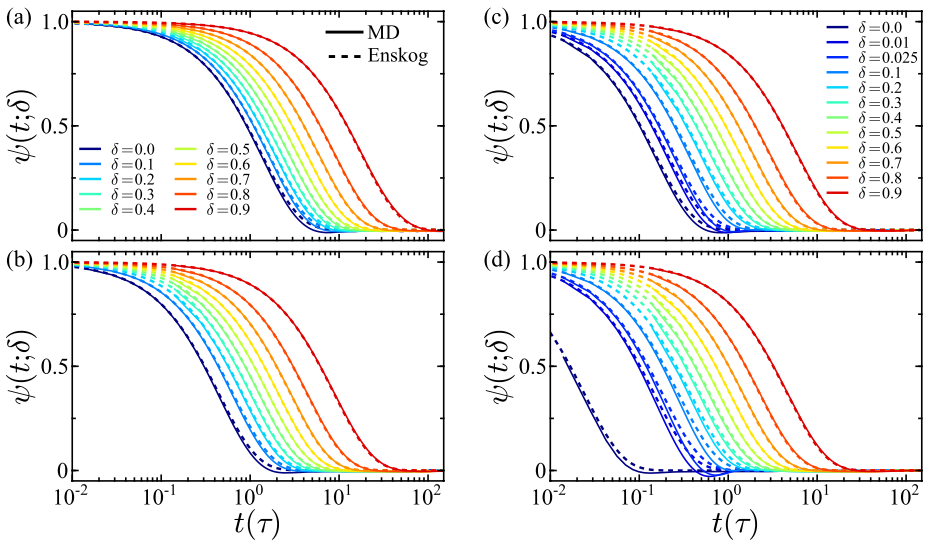

FIG. 7. Semi-log plots of the velocity autocorrelation $\psi(t;\delta)$ for various values of δ at (a) $\phi_0 = 0.25$, (b) $\phi_0 = 0.5$, (c) $\phi_0 = 0.75$, and (d) $\phi_0 = 0.95$. The solid curves are the results measured from MD simulations. The dashed curves are the Enskog results $\psi_E(\delta;t)$ given by Eq. (27). The x-axis shows time in reduced units t/τ.

in the large-δ regime. This is caused by the anticorrelation of collision events as δ is increased toward the completely uncorrelated ideal $\delta = 1$ limit.

As illustrated in Fig. 7(d), for $\phi_0 = 0.95$ and $\delta \in \{0.01, 0.025\}$, $\psi(t)$ becomes more anticorrelated after the initial exponential decay than for the HR ($\delta = 0$) case. This phenomenon can be explained through density-dependent effects in the PMF. At large-ϕ_0 and small-δ, many sets of particles become trapped in a clustered state. Any given particle of such sets can escape the penetrative region only by surmounting a large energy barrier $\Delta V = w_2(\sigma^-; \delta) - w_2(0; \delta)$, which occurs rarely at best.[50] Thus, many sets of particles remain in a clustered state for long times. The onset of these clusters, which are only observed in the small-δ regime, also gives rise to the observed increase in anticorrelation with respect to the HR case.

C. Diffusion coefficient

From the Green-Kubo relation, the diffusion coefficient of a one-dimensional system can be expressed in terms of the VACF as

$$D = \int_0^\infty \langle v_x(0) v_x(t) \rangle \, dt. \tag{28}$$

To quantify the effect that the VACF negative tail has on the diffusion coefficient, Eq. (28) can be separated into two parts: a positive contribution D_+ and a negative contribution D_-. The negative contribution arises over the domain of $\psi(t; \delta)$ with the negative tail. The total diffusion coefficient is the sum of these contributions, $D = D_+ + D_-$.

The positive contribution is computed by integrating the VACF measured from simulation up to the time t_c when its sign first changes from positive to negative

$$D_+ = \int_0^{t_c} \langle v_x(0) v_x(t) \rangle \, dt. \tag{29}$$

At short times, the VACF in Fig. 7 was seen to be well approximated by the exponential Enskog theory. This suggests that the positive contribution to the diffusion coefficient can be approximated by

$$D_+(\delta) \approx \frac{k_B T}{m} \int_0^\infty e^{-2\omega_h(\delta) t} dt. \tag{30}$$

As can be seen in Fig. 8(a), Eq. (30) is in agreement with results obtained by integration of Eq. (29) over all parameter values assessed here. That is, the short-time behavior of $\psi(t; \delta)$ is strongly exponential for all values of δ.

Comparing the measured values for D, shown in Fig. 8(b), with the measured values for D_+, it can be seen that the negative tail, and thus D_-, contributes significantly to the total diffusion coefficient. This effect persists for small-δ regimes but is less severe for large values of δ as collisions become less correlated. It can also be observed in Fig. 8(b) that the result for D computed using the Einstein relation from the measured mean-square displacement is in agreement with the values computed from the measured VACF. For large values of δ, D is approximately linear in density which is the same general trend observed in Fig. 6 for the collision frequency. Figure 9 shows the ratio of theoretically predicted to numerically measured

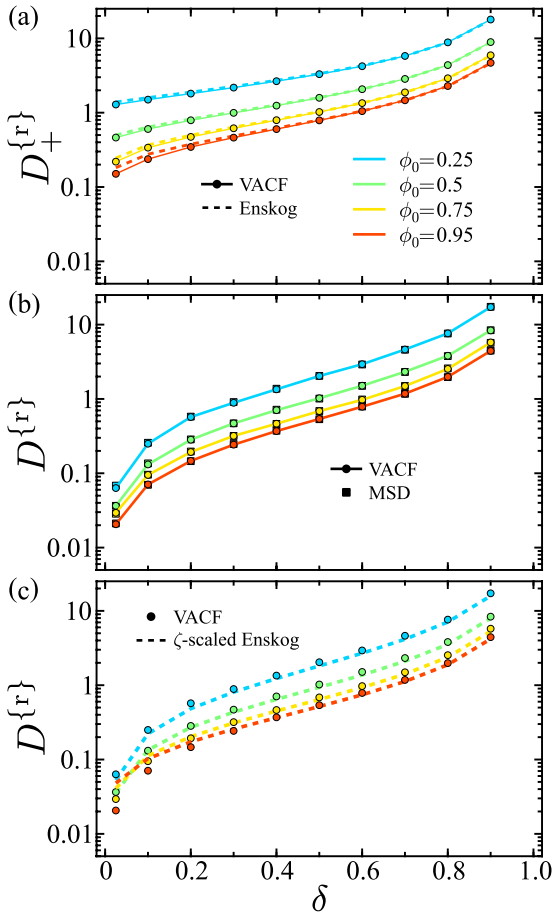

FIG. 8. The positive $D_+^{\{r\}} = D_+/\sigma\sqrt{k_B T/m}$ and total $D^{\{r\}} = D/\sigma\sqrt{k_B T/m}$ reduced diffusion coefficients as a function of the softness parameter are shown above. Diffusion coefficients are shown for $\phi_0 = 0.25$ (blue), $\phi_0 = 0.5$ (green), $\phi_0 = 0.75$ (yellow), and $\phi_0 = 0.95$ (red) as indicated in the legend. Those values computed from the VACF in MD simulations are shown as solid curves with circular markers. The dashed curves in panel (a) are the theoretical Enskog results given by Eq. (30). The square markers in panel (b) correspond to values obtained from the mean square displacement. The dashed curve in panel (c) corresponds to the ζ-scaled Enskog result obtained empirically from g_2.

diffusion coefficients D_t/D_n, where the value of D_t is calculated using Eq. (30). In the small-δ regime, this ratio ranges from approximately 10 to 20, decreasing with increasing ϕ_0. Monotonically decreasing behavior is observed with increasing δ

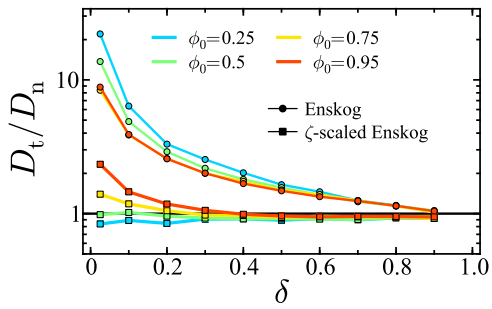

FIG. 9. Semi-log plot of the ratio of the theoretically predicted to numerically measured diffusion coefficients D_t/D_n as a function of δ for $\phi_0 = 0.25$ (blue), $\phi_0 = 0.5$ (green), $\phi_0 = 0.75$ (yellow), and $\phi_0 = 0.95$ (red). The solid curves with circular markers correspond to the results for D_t predicted by the Enskog expression evaluated using empirical values of g_2. The solid curves with square markers correspond to the results for D_t predicted by the ζ-scaled Enskog expression evaluated using empirical values of g_2.

suggesting that as the completely uncorrelated ideal limit is approached, the Enskog approximation becomes more valid. This ratio of diffusion coefficients decreases to $\lessapprox 2$ for $\delta > 0.4$ over all values of ϕ_0.

The exponential Enskog estimate for the correlation function $\psi(t)$ does not account for the negative tail and hence, it leads to an overestimate for D. Based on heuristic arguments, we expect that multi-body effects contribute to the appearance of anticorrelated decay and these effects can be accounted for using the mapping $\delta \mapsto \zeta_0$. Combining Eqs. (16), (27), and (28), we arrive at an expression for the diffusion coefficient,

$$D_\zeta(\delta) = \zeta_0(\delta)\left(\frac{k_B T}{m}\int_0^\infty e^{-2\omega_h(\delta)t}dt\right), \tag{31}$$

which we refer to as the ζ-scaled Enskog result. Figure 8(c) illustrates the agreement observed between the ζ-scaled diffusion coefficient and the diffusion coefficient measured from simulation using Eq. (28). As shown in Fig. 9, for D_t calculated using Eq. (31), D_t/D_n ranges between 0.85 and 1.18 for $\delta > 0.2$ over all values of ϕ_0. For $\delta < 0.2$, a maximum ratio of 2.2 is observed at $\phi_0 = 0.95$ and $\delta = 0.01$. For all other parameter values in the small-δ regime, the ratio ranges between 0.84 and 1.45. Thus, the Enskog expression with included ζ-scaling gives an excellent approximation for D.

V. SEQUENTIAL ORDER AND MIXING RATES

A distinguishing feature of penetrable-rod systems, relative to the HR case, is that particles can move through each other and the configuration-space order of particles $r_1 < r_2 < r_3 \cdots < r_N$ is not maintained. Jepsen's derivation for the VACF of hard point particles relies on the persistence of this monotonic order. In a HR system, a particle at position i in this ordering only exchanges velocities with the particles at either the $i-1$ or $i+1$ nearest-neighbor positions. Knowledge of the decay of this sequence of exchanges allows for an exact solution to the non-stationary distributions defining the dynamical observables.[46] However, when particles are allowed to penetrate due to boundedness in the intermolecular potential, the ordering of particles will not be maintained. Thus, for any collision event, the particle at the position i can exchange velocities with any other particle. Moreover, during soft collision events the order of the particles can be altered. The dynamics of a particle in a penetrable system is thus entangled with all other particles.

As an example of a change in order, consider a set of $N = 7$ rods, ordered by position, with the location of an arbitrary rod chosen as the origin. The corresponding order of particle indices at an arbitrarily chosen initial time t_0 generates the sequence order

$$O(t_0) = \{1,2,3,4,5,6,7\}.$$

In a HR system, for all t, $O(t) = O(t_0)$ as this sequence will never change. Representative configurations for the initial configurations of penetrable ($\delta > 0$) systems are shown in Figs. 10(a) and 10(d). After propagating the system for the time $t_1 - t_0$, the sequence of indices ordered by position will be altered due to interpenetration of the rods. A representative spatial configuration and sequence,

$$O(t_1) = \{1,3,5,7,2,4,6\},$$

generated after this evolution is shown in Fig. 10(b). The manner and degree to which dynamical observables are correlated to sequential order provides a route to determining the kinetic properties in a physically relevant space that differs from either configuration or phase spaces.

To develop an observable metric, we examine the rate of mixing of the modular distance between nearest neighbors in sequential space. The modular distance between a pair of particles at positions i and $i+1$ in a sequence O is given by

$$\mathcal{M}_i(N, O_i, O_{i+1}) = \min(|O_i - O_{i+1}|, N - |O_i - O_{i+1}|), \tag{32}$$

where the subscript indices are mod N with offset 1, i.e, $i = N + 1 = 1$, to account for periodic boundary conditions. The average value of $\mathcal{M}$ for the sequence state O is

$$\Omega^s(N) = \frac{1}{N}\sum_{i=1}^{N}\mathcal{M}_i(N, O_i, O_{i+1}), \tag{33}$$

which can be used to quantify and compare the degree of sequential order for differing sequences. Moreover, the nearest neighbor adjacency matrix

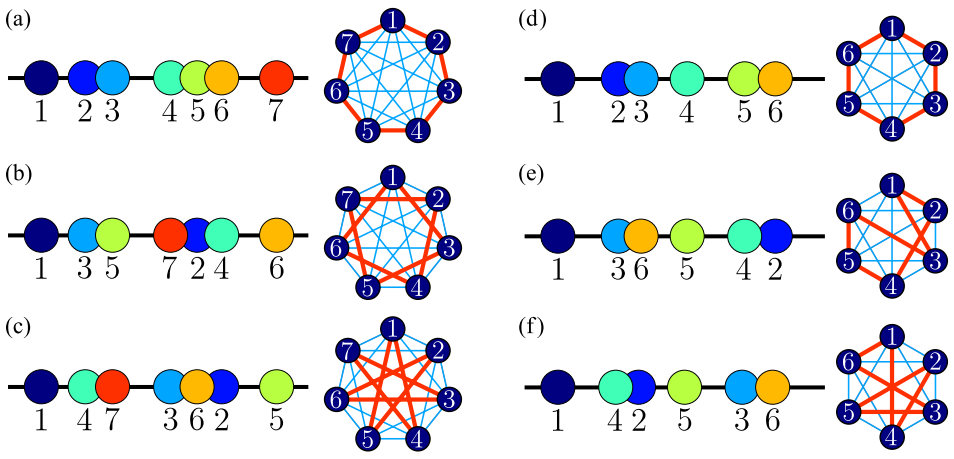

FIG. 10. Representative spatial and sequential configurations for a system evolving through Eq. (2). Panels (a), (b), and (c) show spatial configurations (left) generating the sequences O (shown below) for minimum, arbitrary, and maximum values, respectively, of Ω. In each spatial configuration, the particles are colored according to the sequential index. These configurations are shown for $N = 7$, representing the cases where N is odd. Shown to the right in each panel is the corresponding graph $\mathbf{O}(t)$ in which each node corresponds to a specific particle, as marked, and the red lines show the connection to the nearest neighbor. Panels (d), (e), and (f) show the corresponding configurations for $N = 6$, representing the cases where N is even.

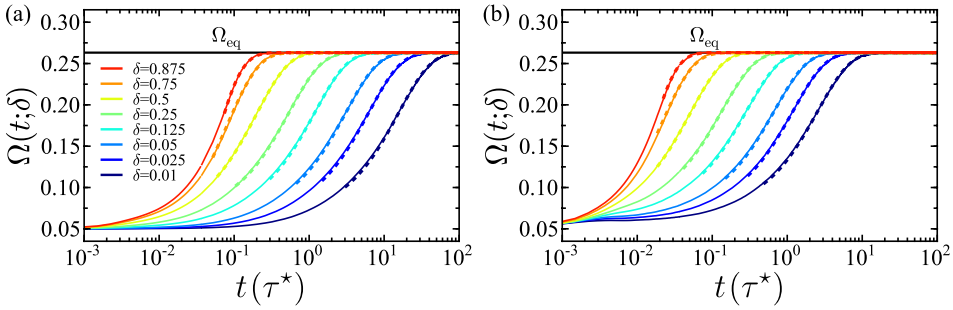

FIG. 11. Semi-log plot illustrating the time dependence of Ω with $N = 20$ for (a) $\phi_0 = 0.25$ and (b) $\phi_0 = 0.95$. Results are shown for various values of δ. The solid black line denotes the value of Ω_{eq}. The solid curves are the results measured from MD simulations and the dashed curves show the results of the exponential portion of the data, fit to Eq. (43). The x-axis shows time in reduced units $t/\tau^\star$ with $\tau^\star = \tau N(N-1)/2$.

$$\mathbf{O}(t) = \begin{pmatrix} o_{11} & o_{12} & \cdots & o_{1N} \\ o_{21} & o_{22} & \cdots & o_{2N} \\ \vdots & \vdots & \ddots & \vdots \\ o_{N1} & o_{N2} & \cdots & o_{NN} \end{pmatrix}, \tag{34}$$

where $o_{ij} = 1$ if the particles are neighboring and $o_{ij} = 0$ otherwise, is a sparse array defining the connection to nearest neighbors. Representative examples for $\mathbf{O}(t)$ are shown to the right in all panels in Fig. 10, corresponding to the sequences shown to the left in the same figure. Equation (34) differs from Eq. (3) as $\mathbf{S}(t)$ defines the total connection network and $\mathbf{O}(t)$ only represents connections to nearest neighbors.

The minimum value of Ω^s is obtained when each $\mathcal{M}_i$ holds its minimum value. Scaling this value by the system size N gives

$$\Omega^s_{\min} = \frac{1}{N}. \tag{35}$$

This minimum value is maintained throughout the course of a simulation of HRs as the particles will never mix and the sequential order is always maintained. As the thermodynamic limit is approached,

$$\lim_{N\to\infty} \Omega^s_{\min} = 0. \tag{36}$$

Defining the ensemble average over all Ω^s as Ω, at time t_0, $\Omega_{\min} = \Omega^s_{\min}$. For the purpose of examining the time-dependence of Ω, we define each trajectory to begin in the ordered state giving $\Omega^s_{\min}$. Representative spatial and sequential configurations $\Omega^s_{\min}$ are shown in Figs. 10(a) and 10(d) for odd and even N, respectively.

After evolution of the ensemble, and interpenetration of particles, the particle sequence can be altered from its initial order. The ensemble average at equilibrium Ω_{eq} is achieved when the probability for each possible value of $\mathcal{M}_i$ is uniform, subject to parity conditions. This result can be derived by considering a dummy particle and averaging over all possible values of $\mathcal{M}$. Generating each of these values as follows: for each of two nearest neighbor positions $\mathcal{M} = 1$, for each of two *next* nearest neighbor positions $\mathcal{M} = 2$, etc., allows construction of the relevant distribution. If N is even, there is single value $\mathcal{M}_{N/2} = N/2$ that must be included. The summation of this sequence over the respective bounds, scaled by a factor $1/N$, can be expressed as

$$\Omega_{eq} = \frac{1}{N(N-1)}\left(\sum_{k=1}^{\frac{N}{2}-1} 2k + \frac{N}{2}\right), \tag{37}$$

if N is even, and

$$\Omega_{eq} = \frac{1}{N(N-1)}\left(\sum_{k=1}^{\frac{N-1}{2}} 2k\right), \tag{38}$$

if N is odd. Evaluating these sums gives

$$\Omega_{eq} = \begin{cases} \dfrac{N^2}{4N(N-1)}, & \text{if } N \text{ is even} \\ \dfrac{N+1}{4N}, & \text{if } N \text{ is odd} \end{cases}, \tag{39}$$

and at the thermodynamic limit,

$$\lim_{N\to\infty} \Omega_{eq} = \frac{1}{4}. \tag{40}$$

It can be immediately observed that Ω will increase from a value $\Omega_{\min}$ at an arbitrarily chosen initial time to Ω_{eq} as $t \to \infty$ and the equilibrium mixed state is approached. Configurations that contribute to Ω_{eq} are shown in Figs. 10(b) and 10(e) for odd and even cases. Additionally, the maximum value Ω^s can take is

$$\Omega^s_{\max} = \begin{cases} \dfrac{N^2-2N+4}{2N^2}, & \text{if } N \text{ is even} \\ \dfrac{N-1}{2N}, & \text{if } N \text{ is odd} \end{cases}, \tag{41}$$

which in the thermodynamic limit is

$$\lim_{N\to\infty} \Omega^s_{\max} = \frac{1}{2}. \tag{42}$$

The result for $\Omega^s_{\max}$ in the case where N is odd is trivial and is achieved when each $\mathcal{M}_i$ holds the maximum value $(N-1)/2$. For the case when N is even, the result for $\Omega^s_{\max}$ is stated without proof, but has been confirmed by generating $\Omega^s_{\max}$ through genetic optimization of O. Shown in Figs. 10(c) and 10(f) are configurations generating $\Omega^s_{\max}$ for example systems.

The sequential order parameter Ω increases in time from an initial value $\Omega_{\min}$ to an equilibrium value Ω_{eq}. The equilibrium state maximizes the information entropy of O and represents a completely mixed system in sequential space. Assuming that the kinetics of this process are first-order gives

$$\Omega(t;\delta) = -Ce^{-k_\Omega(\delta)t} + \Omega_{eq}, \tag{43}$$

where k_Ω is the sequential mixing rate constant and Ω_{eq} is the equilibrium value, given by Eq. (39). Equation (43) agrees with our known physical criterion that $\Omega(t;\delta)$ increases to Ω_{eq} as $t \to \infty$. The rate of this process is an extensive property, increasing in N, and is proportional to the number of connections, and thus possible interactions in the collision network.

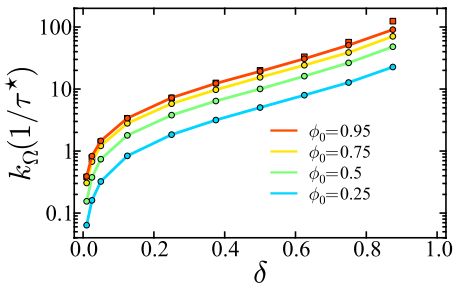

FIG. 12. Semi-log plot of the sequential mixing rate constant k_Ω as a function of δ. The solid curves with circular markers are the results measured for a system of $N = 20$ particles and various ϕ_0 values, as marked. The square markers are the results obtained for $N = 100$ particles at $\phi_0 = 0.95$. The y-axis shows the rates in reduced units $\tau^\star/t$ with $\tau^\star = \tau N(N-1)/2$.

Thus, to compare mixing rates for different values of N, time must be scaled by a factor $N(N-1)/2$ removing the extensive time-dependence of k_Ω.

To measure k_Ω from simulation, $\Omega(t;\delta)$ was calculated over at least 8000 trajectories for each parameter set $\{\phi_0, \delta\}$ as required to achieve convergence. The rate constant was obtained by fitting the data to Eq. (43). As shown in Fig. 11, after an initial relaxation period, the time-dependence of $\Omega(t;\delta)$ is strongly exponential. Interestingly, for large δ close to the ideal limit the early-time kinetics are zeroth order, being linear in time. At this limit, the trajectories of all particles become uncorrelated and the system quickly decays to a disordered state. However, the persistence of exponential behavior is observed for this regime in the long-time limit.

An increase in the sequential mixing rate with increasing density ϕ_0 is observed in Fig. 12. This results from corresponding increases in the soft collision frequency. Comparison between the trends for k_Ω and the diffusion coefficient D shown in Fig. 8 suggests that an increasing rate of sequential mixing leads to a decreasing diffusion coefficient. Moreover, the forms of both D and k_Ω as functions of δ are qualitatively correlated, and both exhibit highly non-linear behavior in the small-δ regime. A conjecture, supported by this correlation, is that the diffusion coefficient can be derived purely from knowledge of the decay of sequential order. It originates from the observed correspondence in the relaxation dynamics with respect to the physical configuration or phase space, and the sequence space.

VI. CONCLUSIONS

The dynamical properties of a system of penetrable rods constrained to move on a line in one dimension governed by stochastic intermolecular interactions have been studied over varying ranges of penetrability and softness. We have shown that through a single softness parameter, the limiting dynamical regimes can be bridged. Various dynamical observables were determined from simulation and found to compare favorably to theory. While the spatial structures of stochastic soft-matter systems are highly complex, the dynamical properties can be adequately approximated using modified hard-core arguments with Enskog corrections. The decay time constants vary with the degree of softness, but the relaxation profiles exhibit the same shape in all the cases observed here. This suggests that SHC dynamics are dictated predominantly by energy transfer at collisions.

Open questions remain as to the best methodology for mapping the kinetic distributions of coarse-grained structures to the dynamics of the decimated all-atom systems. While it is well-known that coarse-graining can indeed reproduce the spatial distributions of all-atom systems,[3,63–65] understanding the coarse-grained dynamical mapping has been elusive.[32] A derivation of the exact mapping operator that reproduces the all-atom Hamiltonian dynamics in the coarse-grained space would have large implications for computational science as well as for our understanding of the hierarchy of length scales when moving from the microscopic to the macroscopic scale. The stochastic interactions presented in this article allow for parametrized control of correlation between structures, bridging the completely correlated and completely uncorrelated limits.

Extending the current single-length-scale system to a system with multiple length scales[66] provides for possible future directions of the present work. Barkan *et al.*[67] have shown that the controlled assembly of particles interacting through bounded potentials with multiple length scales allows the generation of structures with periodic and aperiodic lattice geometries, including quasi-crystalline phases. Archer *et al.* have shown that in a system of two-length-scale, soft-core (bounded) particles, there exists a crystal-liquid state as characterized by a set of mobile particles inside a lattice structure.[68] Extending the SHC model to have multiple regions of stochastic penetration could give rise to similar structural behavior and allow for probing such systems at constant temperature.

The application of stochastic bounded potentials to model mesoscale behavior of particles at higher dimensionalities—such as disks or spheres—provides another possible path forward. Our current (unpublished) work suggests that the expressions derived here can be scaled with dimensionality. Comparing them to simulation results could provide insight into the dynamical properties of coarse-grained particles at higher dimensionalities.

ACKNOWLEDGMENTS

This work has been partially supported by the National Science Foundation (NSF) through Grant No. NSF-CHE-1112067.

[1]J. F. Dama, A. V. Sinitskiy, M. McCullagh, J. Weare, B. Roux, A. R. Dinner, and G. A. Voth, "The theory of ultra-coarse-graining. 1. General principles," J. Chem. Theory Comput. **9**, 2466–2480 (2013).

[2]M. G. Saunders and G. A. Voth, "Coarse-graining methods for computational biology," Annu. Rev. Biophys. **42**, 73–93 (2013).

[3]A. Davtyan, J. F. Dama, A. V. Sinitskiy, and G. A. Voth, "The theory of ultra-coarse-graining. 2. Numerical implementation," J. Chem. Theory Comput. **10**, 5265–5275 (2014).

[4]C. N. Likos, "Soft matter with soft particles," Soft Matter **2**, 478–498 (2006).

[5]F. Stillinger, "Phase transitions in the Gaussian core system," J. Chem. Phys. **65**, 3968–3974 (1976).

[6]H. Graf and H. Löwen, "Density jumps across phase transitions in soft-matter systems," Phys. Rev. E **57**, 5744–5753 (1998).

[7]M. Schmidt and M. Fuchs, "Penetrability in model colloid–Polymer mixtures," J. Chem. Phys. **117**, 6308–6312 (2002).

[8]C. N. Likos, S. Rosenfeldt, N. Dingenouts, M. Ballauff, P. Lindner, N. Werner, and F. Vogtle, "Gaussian effective interaction between flexible dendrimers of fourth generation: A theoretical and experimental study," J. Chem. Phys. **117**, 1869–1877 (2002).

[9]B. M. Mladek, M.-J. Fernaud, G. Kahl, and M. Neumann, "On the thermodynamic properties of the generalized Gaussian core model," Condens. Matter Phys. **8**, 135–148 (2005).
[10]B. M. Mladek, D. Gottwald, G. Kahl, M. Neumann, and C. N. Likos, "Formation of polymorphic cluster phases for a class of models of purely repulsive soft spheres," Phys. Rev. Lett. **96**, 045701 (2006).
[11]C. Zachary, F. Stillinger, and S. Torquato, "Gaussian core model phase diagram and pair correlations in high Euclidean dimensions," J. Chem. Phys. **128**, 224505 (2008).
[12]J. C. Pamies, A. Cacciuto, and D. Frenkel, "Phase diagram of Hertzian spheres," J. Chem. Phys. **131**, 044514 (2009).
[13]A. Narros, A. J. Moreno, and C. N. Likos, "Influence of topology on effective potentials: Coarse-graining ring polymers," Soft Matter **6**, 2435–2441 (2010).
[14]W. G. Noid, "Perspective: Coarse-grained models for biomolecular systems," J. Chem. Phys. **139**, 090901 (2013).
[15]C. Marquest and T. Witten, "Simple cubic structure in copolymer mesophases," J. Phys. **50**, 1267–1277 (1989).
[16]A. Ikeda and K. Miyazaki, "Glass transition of the monodisperse Gaussian core model," Phys. Rev. Lett. **106**, 015701 (2011).
[17]D. Coslovich and A. Ikeda, "Cluster and reentrant anomalies of nearly Gaussian core particles," Soft Matter **9**, 6786–6795 (2013).
[18]N. B. Wilding and P. Sollich, "Demixing cascades in cluster crystals," J. Chem. Phys. **141**, 094903 (2014).
[19]S. Prestipino and F. Saija, "Hexatic phase and cluster crystals of two-dimensional GEM4 spheres," J. Chem. Phys. **141**, 184502 (2014).
[20]D. Chandler, J. Weeks, and H. Andersen, "Van der Waals picture of liquids, solids, and phase transformations," Science **220**, 787–794 (1983).
[21]A. V. Popov, J. Melvin, and R. Hernandez, "Dynamics of swelling hard spheres surmised by an irreversible Langevin equation," J. Phys. Chem. A **110**, 1635–1644 (2006).
[22]A. Santos, "Class of consistent fundamental-measure free energies for hard-sphere mixtures," Phys. Rev. E **86**, 040102(R) (2012).
[23]A. Malijevsky and A. Santos, "Structure of penetrable-rod fluids: Exact properties and comparison between Monte Carlo simulations and two analytic theories," J. Chem. Phys. **124**, 074508 (2006).
[24]A. Santos and A. Malijevskỳ, "Radial distribution function of penetrable sphere fluids to the second order in density," Phys. Rev. E **75**, 021201 (2007).
[25]A. Malijevskỳ, S. Yuste, and A. Santos, "Low-temperature and high-temperature approximations for penetrable-sphere fluids: Comparison with Monte Carlo simulations and integral equation theories," Phys. Rev. E **76**, 021504 (2007).
[26]S. Suh, C. Kim, S. Kim, and A. Santos, "Molecular dynamics simulation study of self-diffusion for penetrable-sphere model fluids," Phys. Rev. E **82**, 051202 (2010).
[27]N. Choudhury and S. Ghosh, "Integral equation theory of penetrable sphere fluids: A modified Verlet bridge function approach," J. Chem. Phys. **119**, 4827–4832 (2003).
[28]L. Viererblová, J. Kolafa, S. Labík, and A. Malijevskỳ, "Virial coefficients and equation of state of the penetrable sphere model," Phys. Chem. Chem. Phys. **12**, 254–262 (2010).
[29]C. Likos, M. Watzlawek, and H. Löwen, "Freezing and clustering transitions for penetrable spheres," Phys. Rev. E **58**, 3135–3144 (1998).
[30]B. M. Mladek, P. Charbonneau, C. N. Likos, D. Frenkel, and G. Kahl, "Multiple occupancy crystals formed by purely repulsive soft particles," J. Phys.: Condens. Matter **20**, 494245 (2008).
[31]K. Zhang and P. Charbonneau, "$[N]pT$ Monte Carlo simulations of the cluster-crystal-forming penetrable sphere model," J. Chem. Phys. **136**, 214106 (2012).
[32]M. C. Hagy and R. Hernandez, "Dynamical simulation of dipolar Janus colloids: Dynamical properties," J. Chem. Phys. **138**, 184903 (2013).
[33]J. K. Brennan, M. Lsal, J. D. Moore, S. Izvekov, I. V. Schweigert, and J. P. Larentzos, "Coarse-grain model simulations of nonequilibrium dynamics in heterogeneous materials," J. Phys. Chem. Lett. **5**, 2144–2149 (2014).
[34]A. Malevanets and R. Kapral, "Mesoscopic model for solvent dynamics," J. Chem. Phys. **110**, 8605–8613 (1999).
[35]A. Malevanets and R. Kapral, "Solute molecular dynamics in a mesoscale solvent," J. Chem. Phys. **112**, 7260–7269 (2000).
[36]G. T. Craven, A. V. Popov, and R. Hernandez, "Stochastic dynamics of penetrable rods in one dimension: Occupied volume and spatial order," J. Chem. Phys. **138**, 244901 (2013).
[37]G. T. Craven, A. V. Popov, and R. Hernandez, "Structure of a tractable stochastic mimic of soft particles," Soft Matter **10**, 5350–5361 (2014).
[38]B. Sutherland, "Exact solution for the time evolution of a one-dimensional system," Phys. Rev. A **21**, 2130–2135 (1980).
[39]C. Foidl, "Exact pair distribution function and structure factor for a one-dimensional hard rod mixture," J. Chem. Phys. **85**, 410–417 (1986).
[40]C. Speranza, S. Prestipino, and P. Giaquinta, "Thermodynamic and structural anomalies of the Gaussian-core model in one dimension," Mol. Phys. **109**, 3001–3013 (2011).
[41]S. Prestipino, "Cluster phases of penetrable rods on a line," Phys. Rev. E **90**, 042306 (2014).
[42]L. Tonks, "The complete equation of state of one, two and three-dimensional gases of hard elastic spheres," Phys. Rev. **50**, 955–963 (1936).
[43]J. Lebowitz and J. Percus, "Kinetic equations and density expansions: Exactly solvable one-dimensional system," Phys. Rev. **155**, 122 (1967).
[44]J. Lebowitz, J. Percus, and J. Sykes, "Time evolution of the total distribution function of a one-dimensional system of hard rods," Phys. Rev. **171**, 224 (1968).
[45]J. Lebowitz and J. Sykes, "The velocity autocorrelation function of a finite model system," J. Stat. Phys. **6**, 157–171 (1972).
[46]D. Jepsen, "Dynamics of a simple many-body system of hard rods," J. Math. Phys. **6**, 405 (1965).
[47]M. Bishop and B. Berne, "Molecular dynamics of one-dimensional hard rods," J. Chem. Phys. **60**, 893–897 (1974).
[48]J. Haus and H. Raveché, "Computer studies of dynamics in one dimension: Hard rods," J. Chem. Phys. **68**, 4969–4976 (1978).
[49]I. Gallagher, L. Saint-Raymond, and B. Texier, "From Newton to Boltzmann: Hard spheres and short-range potentials," *Zurich Lectures in Advanced Mathematics* (European Mathematical Society, Zurich, 2014).
[50]G. T. Craven, A. V. Popov, and R. Hernandez, "Effective surface coverage of coarse-grained soft matter," J. Phys. Chem. B **118**, 14092–14102 (2014).
[51]Z. Salsburg, R. Zwanzig, and J. Kirkwood, "Molecular distribution functions in a one-dimensional fluid," J. Chem. Phys. **21**, 1098–1107 (1953).
[52]A. Mattuck, *Introduction to Analysis* (Prentice Hall, New Jersey, 1999).
[53]S. Torquato, *Random Heterogenous Materials: Microstructure and Macroscopic Properties* (Springer-Verlag, New York, 2002).
[54]J. Mittal, J. R. Errington, and T. M. Truskett, "Quantitative link between single-particle dynamics and static structure of supercooled liquids," J. Phys. Chem. B **110**, 18147–18150 (2006).
[55]J. R. Errington, T. M. Truskett, and J. Mittal, "Excess-entropy-based anomalies for a waterlike fluid," J. Chem. Phys. **125**, 244502 (2006).
[56]W. P. Krekelberg, T. Kumar, J. Mittal, J. R. Errington, and T. M. Truskett, "Anomalous structure and dynamics of the Gaussian-core fluid," Phys. Rev. E **79**, 031203 (2009).
[57]W. P. Krekelberg, J. Mittal, V. Ganesan, and T. M. Truskett, "How short-range attractions impact the structural order, self-diffusivity, and viscosity of a fluid," J. Chem. Phys. **127**, 044502 (2007).
[58]B. J. Alder and T. E. Wainwright, "Decay of the velocity autocorrelation function," Phys. Rev. A **1**, 18–21 (1970).
[59]B. J. Alder and T. E. Wainwright, "Studies in molecular dynamics. I. General method," J. Chem. Phys. **31**, 459–466 (1959).
[60]S. Suh and H. Liu, "A modified Enskog-like equation of self-diffusion coefficients for penetrable-sphere model fluids," Bull. Korean Chem. Soc. **32**, 1336–1340 (2011).
[61]P. Cutchis, H. van Beijeren, J. R. Dorfman, and E. A. Mason, "Enskog and van der Waals play hockey," Am. J. Phys. **45**, 970–977 (1977).
[62]D. Frenkel and B. Smit, *Understanding Molecular Simulation: From Algorithms to Application* (Academic Press, NY, 1996).
[63]S. Izvekov and G. A. Voth, "Multiscale coarse graining of liquid-state systems," J. Chem. Phys. **123**, 134105 (2005).
[64]M. C. Hagy and R. Hernandez, "Dynamical simulation of dipolar janus colloids: Equilibrium structure and thermodynamics," J. Chem. Phys. **137**, 044505 (2012).
[65]L. Lu, J. F. Dama, and G. A. Voth, "Fitting coarse-grained distribution functions through an iterative force-matching method," J. Chem. Phys. **139**, 121906 (2013).
[66]T. Dotera, T. Oshiro, and P. Ziherl, "Mosaic two-lengthscale quasicrystals," Nature **506**, 208–211 (2014).
[67]K. Barkan, M. Engel, and R. Lifshitz, "Controlled self-assembly of periodic and aperiodic cluster crystals," Phys. Rev. Lett. **113**, 098304 (2014).
[68]A. J. Archer, A. M. Rucklidge, and E. Knobloch, "Quasicrystalline order and a crystal-liquid state in a soft-core fluid," Phys. Rev. Lett. **111**, 165501 (2013).